Flow Pattern Analysis over a Delta Wing at Transonic Speed

Tony Di Fabbio *, Eike Tangermann † and Markus Klein ‡
Bundeswehr University Munich, 85577 Neubiberg, Germany

The present work aims to provide an advancement in the prediction of delta wing flow for the understanding of the several flow physics phenomena that occur over the wing particularly at the transonic speed condition. Simulations of vortex-dominated flow around the sharp leading-edge VFE-2 wing have been performed. The SA-based IDDES model is applied in the scale-resolving computations. The sensitivity of the results to temporal and spatial resolution has been addressed and commented upon. The hybrid method results reveal physical aspects which have been seen neither from URANS nor from experimental data with sufficient accuracy. The complex leading-edge vortex pattern, the shock waves locations and subsequently the vortex-shock interaction have been investigated. The grey-area issue have been also assessed.

I. Nomenclature

(U)RANS	=	(Unsteady) Reynolds Averaged Navier-Stokes
IDDES	=	Improved Delayed Detached Eddy Simulation
SA-negRC	=	Spalart-Allmaras One-Equation Model with negative turbulent viscosity and Rotation/Curvature correction
CFL	=	Courant-Friedrichs-Lewy number
CTU	=	Convective Time Unit
x, y, z	=	Cartesian coordinates $[m]$
ξ, η, ψ	=	Dimensionless Cartesian coordinates
Ma	=	Mach number
Re	=	Reynolds number
L	=	Characteristic length $[m]$
V	=	Cell volume $[m^3]$
Δ	=	Characteristic cell size $[m]$
ω_x	=	x-vorticity $[1/s]$
d_ω	=	Vortex diameter based on ω_x $[m]$
N_ω	=	Number of grid points inside vortex diameter d_ω
d	=	RANS length scale $[m]$
$\tilde{d}$	=	Hybrid length scale $[m]$
α	=	Angle of attack $[deg]$
C_L	=	Lift coefficient
C_D	=	Drag coefficient
c_p	=	Pressure coefficient
u, v, w	=	Velocity components $[m/s]$
u_θ	=	In-plane tangential velocity $[m/s]$
U	=	Velocity magnitude $[m/s]$
Q	=	Q-criterion $[1/s^2]$
H_n	=	Normalized helicity
$\nabla\rho$	=	Density gradient $[kg/m^4]$
μ	=	Dynamic molecular viscosity $[kg/(ms)]$
μ_t	=	Turbulent eddy viscosity $[kg/(ms)]$
R_t	=	Turbulent eddy viscosity over dynamic molecular viscosity
K	=	Normalized turbulent kinetic energy

*Research Assistant, Institute of Applied Mathematics and Scientific Computing, Department of Aerospace Engineering
†Senior Research Associate, Institute of Applied Mathematics and Scientific Computing, Department of Aerospace Engineering
‡Professor, Institute of Applied Mathematics and Scientific Computing, Department of Aerospace Engineering

II. Introduction

Complex flow fields dominated by vortex systems are generated at extreme flight conditions over low aspect ratio wings with highly swept leading-edges. In order to correctly predict the flow physics over the wing, the treatment of turbulence, which is challenging for numerical simulation, has to be assessed.

Large ranges of computations can be performed by applying the classical RANS models that are very efficient in terms of computational time. However, they are not capable of predicting the flow sufficiently accurate at the evalueted flow conditions. A RANS model, even a complex one, will not provide the accuracy needed in all varieties of vortical, highly unsteady, flows. Different approaches could be found in literature in order to overcome the deficiencies of the RANS approach, such as the Reynolds-stress models and the Quadratic Constitutive Relation. Moioli et al. [1] for example aimed to adapt a turbulence model to a specific application, by using an experimental database to improve the results of the one equation SA model.

On the other hand, resolving turbulence employing Large Eddy Simulation (LES) is far too expensive in terms of computational effort to apply it on a routine basis. For this reason, instead of modeling the entire turbulent spectrum, the hybrid RANS/LES approach becomes an alternative to accurately capture the unsteady characteristics of various scale vortices at reasonable effort by resolving different portions of the turbulent spectrum.

RANS and hybrid RANS-LES computations were carried out for the flow about the VFE-2 delta wing by Peng and Jirásek [2] at a low-speed subsonic Mach number $Ma = 0.14$ and an angle of attack $\alpha = 23°$. The hybrid RANS-LES computation has reproduced the mean flow in a more reasonable pattern than the RANS computation, conducted with the Spalart-Allmaras (SA) model and an Explicit Algebraic Reynolds Stress Model (EARSM), in view of the resolved secondary vortex and the predicted surface pressure.

Moreover, Cummings and Schütte [3] have performed numerical simulations using RANS and several hybrid turbulence models, of the flow at subsonic condition for the VFE-2 delta wing configuration with rounded leading-edges. The simulated flow field using SA-DDES has been significantly improved over any of the other hybrid turbulence model simulations and the results showed promise for gaining a fuller understanding of the flow field.

Since the DDES model essentially switches to URANS mode in the wall layer, the IDDES approaches has been selected for the scale-resolving simulations in the present work. The generation of the turbulence usually starts quite early on a delta wing that features a sharp leading-edge and it may help to drive the IDDES modelling towards wall-modeled LES mode and thereby benefit from is capability of better resolving turbulence in the shear layer immediately after separation.

Simulations of the sharp leading-edge VFE-2 wing [4] have been performed at transonic conditions with $Ma_\infty = 0.8$, $Re_\infty = 2 \cdot 10^6$ and $\alpha = 20.5°$ using different levels of temporal and spatial resolution, of which results have been compared. The vortex-dominated flow has been investigated in detail comparing IDDES and URANS results with experimental data reference for experiments. The SAneg-based IDDES model is applied in the scale-resolving computations, whereas the Spalart-Allmaras One-Equation Model with corrections for negative turbulent viscosity and Rotation/Curvature (SA-negRC) is employed to close the RANS equations [5]. The simulations have been performed employing the DLR TAU-Code release.2019.1.0 flow solver [6].

The tested flow conditions have been selected taking the several considerations into account. Since the flow separation, which forms the initial stage of vortex formation, is fixed by the sharp leading-edge, the main challenge within the simulation is to correctly produce formation and further development of the vortical flow system along the wing surface, which is primarily affected by the treatment of the turbulence in terms of modeling or resolving turbulent eddies. In case of low aspect ratio delta wings, the shear layer emanating from the leading-edge is rolling up to form a leading-edge vortex over the wing, by inducing additional velocities on the wing surface. The generated vortex sheet is highly influenced by the pressure gradients in its vicinity and its separation at the swept leading-edge causes a local low pressure region on the suction side which contributes to the overall lift [7]. The so-called vortex lift has a limiting AoA at which the vortex bursts or breaks down. This consists of an abrupt change in the flow topology where the flow decelerates and diverges. The flow physics over a delta wing further complicates at transonic conditions because of the presence of single or multiple shock waves and subsequently the interaction between shocks and vortices, which could trigger the appearance of the vortex breakdown. The complex shock-waves and vortex system has been investigated in detail by analysing several details with a promising accuracy.

Finally, the present work aims to provide a better understanding of the vortex-dominated flows particularly at transonic conditions in order to determine the range of suitability of current CFD methods. The main purpose is to provide an advancement in the prediction of delta wing flow for the understanding of the several flow phenomena that occur over the wing. The sensitivity of the results to temporal and spatial resolution has been even addressed and commented upon, leading to important conclusions.

III. Test Case Description

A. Geometry and Mesh

The VFE-2 wing with a leading-edge sweep angle of $\phi = 65°$ features a sharp leading-edge. The experimental data consist of PSP and PIV measurements provided by DLR German Aerospace Center [4]. The dimensionless Cartesian coordinates are introduced as follows

$$\xi = x/L, \quad \eta = y/(x \cdot tan(\phi)), \quad \psi = z/(x \cdot tan(\phi)). \tag{1}$$

Fig. 1 shows the computational domain employed to investigate the VFE-2 geometry. The unstructured mesh consists of about 30 million cells and it is formed by 30 prism layers close to the aircraft and tetrahedral volumes everywhere else. The mesh is symmetric to the plane $y = 0$ but it is not homogeneous, the cells size varies within the computational domain. The finest cells, whose size is around 0.002 times the characteristic length, $\Delta = V^{1/3} \approx 0.002\ L$, are located close to the leading-edge, where the vortices are generated. In order to capture the turbulent fluctuations along the energy cascade the mesh refinement roughly also follows the vortices.

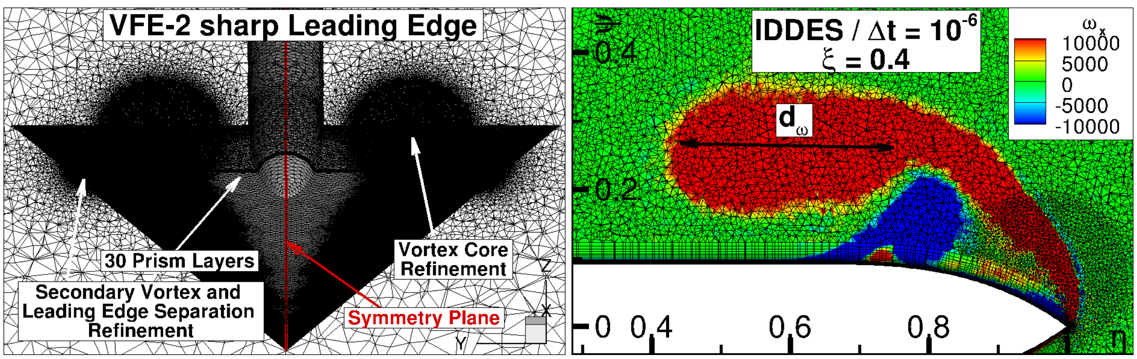

Fig. 1 VFE-2 mesh (left) and vortex diameter $d_\omega[m]$ based on the mean vorticity $\omega_x[1/s]$ (right)

The number of grid points inside the vortex diameter is analysed at chordwise location $\xi = 0.4$, in order to provide a justification that the grid resolution can assumed to be adequate for the given flow. The vortex diameter has been computed from the vorticity distribution ω_x of the vortex, denoted by $d_\omega \approx 0.3L$, as it has been suggested by Landa et al [8]. Figure 1 shows qualitatively the measure of the vortex diameter, indicated by an arrow, and the computational domain at chordwise location $\xi = 0.4$. $N_\omega = d_\omega/\Delta \approx 150$ is the number of grid cells inside the vortex diameter d_ω. Although the cell size slightly increases inside the vortex core along the wing, the ratio of the vortex diameter to the cell size rises due to the vortex expansion.

B. Mesh Convergence Study - URANS and IDDES runs

A grid-resolution study has been performed for the selected test case in order to analyze the grid effects. Table 1 summarizes the main mesh characteristics. The finest cell size has been halved step by step. The URANS have instead been performed with all the four meshes. The IDDES runs have been performed employing the 24M and the 30M (reference) mesh, in order to prove the effectiveness of the grid resolution.

Table 1 Meshes details and lift coefficient results

Mesh Acronym	Finest Cell Size	Tot. Points
10M	0.016 L	10 million
20M	0.008 L	20 million
24M	0.004 L	24 million
30M	0.002 L	30 million

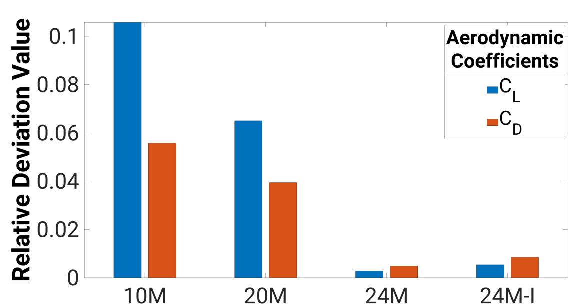

Fig. 2 Relative deviation bar plot

Figure 2* shows the relative deviation of the aerodynamic force coefficients (lift and drag) with respect to the 30M mesh for which results will be presented. Taking both approaches (IDDES and URANS) into account, the plot of the relative deviation demonstrates the reduction of the grid effects. The step towards hybrid RANS/LES is worthwhile even because the "24M-I" column in Fig. 2 shows that there is no relevant difference in the prediction of lift and drag between IDDES results achieved with the 24M and the 30M mesh. This will be confirmed in Section V.B with the analysis of the mean surface coefficient of pressure.

IV. Modeling and Solution

A. CFD equations and approaches

The SA-neg model is based on the following one-equation by Spalart-Allmaras [9] for the eddy viscosity

$$\frac{\partial}{\partial t}(\rho\tilde{\nu}) + \vec{u}\cdot\vec{\nabla}(\rho\tilde{\nu}) = \vec{\nabla}\cdot\left(\frac{\mu+\rho\tilde{\nu}}{\sigma}\vec{\nabla}\tilde{\nu}\right) + \rho\frac{c_{b2}}{\sigma}(\vec{\nabla}\tilde{\nu})^2 + c_{b1}\rho\tilde{S}\tilde{\nu} - c_{w1}f_w\rho\left(\frac{\tilde{\nu}}{\tilde{d}}\right)^2, \tag{2}$$

where the length scale $d = L_{RANS}$ in the destruction term is the distance to the nearest wall [10]. The SA-neg version is used only in order to improve stability and robustness without changing the (converged) results of the SA model. Equation 2 would be modified and the turbulent eddy viscosity in the momentum and energy equations would be set to zero just in case the kinematic eddy viscosity becomes negative [10].

Regarding the URANS runs, the SA turbulence model often provides excessive eddy viscosity production in the vortex, with implications on the unburst vortex size, type and velocities. Shur et al. [11] proposed a streamline curvature correction (SA-RC), applied in the current work just within the URANS computations, which alters the source term with a rotation function. In the RANS context a comparison with and without RC has been preformed resulting in the selection of the SA-negRC model for the presented data as it has produced superior results.

In the IDDES model, instead, d is replaced with $\tilde{d} = L_{IDDES}$, which is defined as

$$\tilde{d} = \tilde{f}_d(1+f_e)d + (1+\tilde{f}_d)C_{DES}\Delta_{max}$$

with $\tilde{f}_d$ the IDDES shielding function, $\Delta_{max} = max(\Delta x, \Delta y, \Delta z)$ and $C_{DES}\Delta = L_{LES}$ [5].

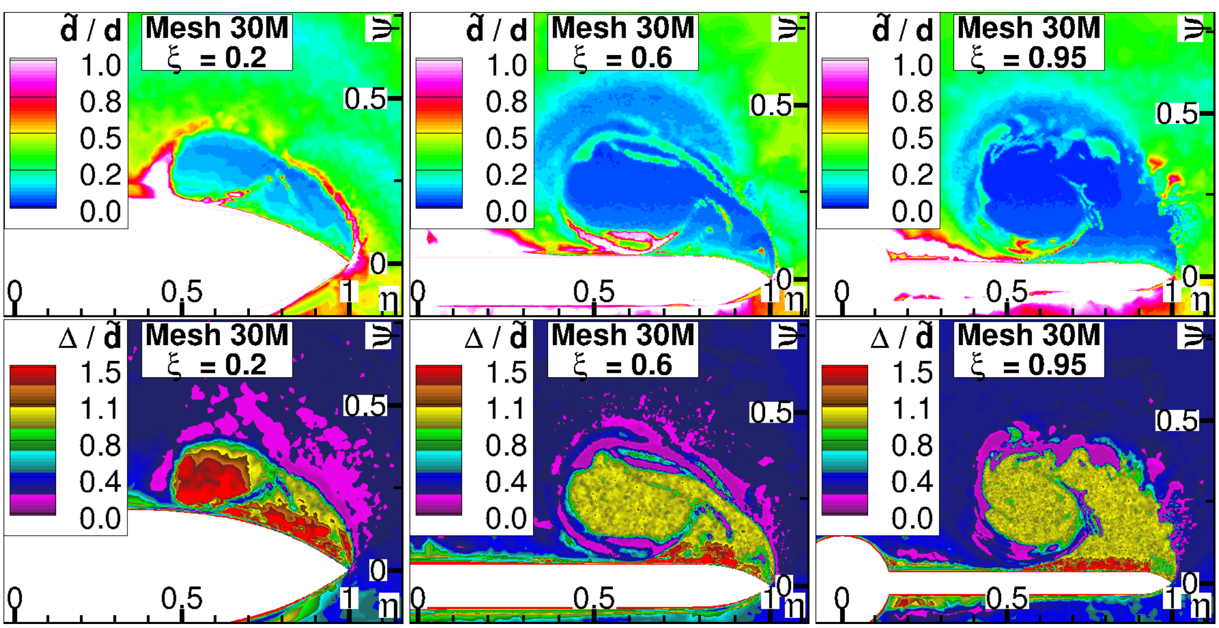

Fig. 3 Instantaneous hybrid length scale over RANS length scale $\tilde{d}/d$ and ratio of cell size to hybrid turbulence scale $\Delta/\tilde{d}$ at chordwise locations $x/L = 0.2,\ 0.6,\ 0.95$, IDDES results with Mesh 30M and $\Delta t = 1e{-}6$

*Left columns are from RANS runs and the "I" denotes IDDES results

Regarding the hybrid RANS/LES runs, Fig. 3 shows the instantaneous hybrid length scale over RANS length scale ($\tilde{d}/d$). It illustrates where the DDES approach switches from RANS to LES. The regions close to the wall are resolved by the RANS mode and a ratio around the unity is expected. In order to complete the discussion about the mesh resolution, Fig. 3 shows also the instantaneous ratio of cell size to hybrid turbulence scale at the same chordwise stations. The ratio is another reliable indicator of the mesh quality and, since it is always around unity in the vortex core, it indicates that the 30M mesh should be able to capture and adequately resolve the turbulence flow structures. The only region to watch out for is is close to the apex, where the ratio is slightly above the unity and where the grey-area issue might affect the results, as it will be discussed in Section V.D.

B. Numerical Approach

An implicit dual-time stepping approach, employing a Backward-Euler/LUSGS implicit smoother, has been used in the unsteady simulations. To ensure convergence of the inner iterations in the IDDES runs, Cauchy convergence criteria of the variables volume averaged turbulent kinetic energy, maximum eddy viscosity, total vorticity, maximum Mach number and certain aerodynamic coefficients with tolerance values of 1e−5 has been applied.

The matrix dissipation model has been selected while performing the computation of the fluxes with a central scheme. However, in hybrid RANS/LES the artificial dissipation should be reduced in order to prevent excessive damping of the resolved turbulent structures. A (hybrid) low-dissipation low-dispersion discretization scheme (LD2) has been used [12].

Regarding the URANS runs, the selected time step size is equal to 1e−4 $s \approx 2.64 \cdot 10^{-2}$ CTU. The convective time unit (CTU) has been computed as follows

$$T = L/U_\infty \approx 3.79 \cdot 10^{-3}\ s = 1\ CTU,$$

where L is the characteristic length and U_∞ the free stream velocity. 10 CTU have been computed before starting the time-averaging in order to overcome the initial transient and 5 flow trough times have been taken into account in order to compute the mean values of the flow proprieties, as it can be seen in Fig. 4 that shows the time history of the lift coefficient C_L and all the described information regarding the time length series.

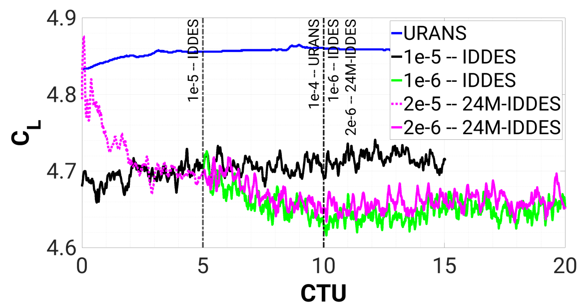

Fig. 4 Time history of the lift coefficient

In order to fully resolve the convective transport and consequently to capture the flow characteristics accurately, the maximum allowed time step size for IDDES has been computed. Taking the IDDES run with the 30M mesh into account, the chosen time step size, Δt = 1e−6 s = 2.64e−4 CTU, adequately resolves the time scales of the energy containing eddies in the flow of interest [13] keeping the convective CFL number lower than unity, as shown in Fig. 5. In order to speed-up the simulation and save computational time, a simulation has been performed increasing the time step up to Δt = 1e−5 s = 2.64e−3 CTU by having a convective CFL number approximately one order higher in magnitude. The IDDES run using the 30M mesh has been initialized from scratch with a steady run and afterwards 5 CTU have been performed with the time step size equal to Δt = 1e−5 s. 10 overflows have been taken into account in order to compute the mean values of the flow properties.

Regarding the IDDES with the time step size equal to Δt = 1e−6 s, after 5 CTU performed with the time step size equal to Δt = 1e−5 s, 5 CTU have been computed with Δt = 1e−6 s before starting the time-averaging, in order to overcome the initial transient. In the end, in this case as well, 10 overflows have been taken into account in order to compute the mean values of the flow properties.

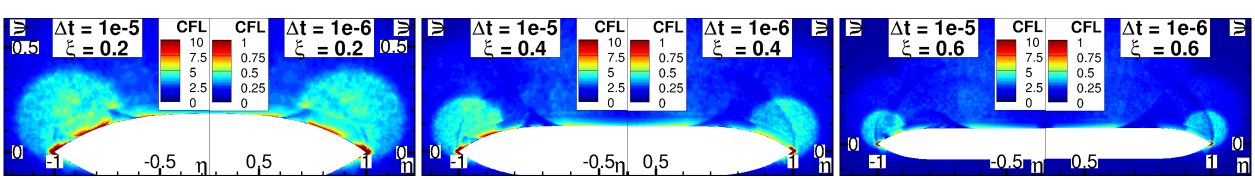

Fig. 5 Mean convective CFL number at chordwise locations $x/L = 0.2,\ 0.6,\ 0.8$, comparison between IDDES results with Δt = 1e−5 s and Δt = 1e−6 s

Finally, Fig. 4 shows the time history of the IDDES run for the 24M mesh as well. These simulations have been initialized with the URANS results and it is important to note that no difference has been found in the duration of the initial transient. It is also worthy to note that the time step sizes have been doubled (see the legend of the Fig. 4) as the size of the finest cell has also been doubled compared to the 30M reference mesh, as summarized in Table 1.

V. Results

The flow physics is described, explained and illustrated in detail by dividing the analysis of the unsteady (instantaneous) flow features (V.A) and the mean flow features (V.B), where several quantities are plotted in order to provide a comparison between the different available data. In Section V.C the vortex flow pattern and the vortex-shock interaction phenomenon will be investigated in detail with the help of the scale-resolving simulation results. Finally, the turbulence-related variables, such as instantaneous eddy viscosity and resolved turbulent kinetic energy will be presented in Section V.D.

A. Unsteady (Instantaneous) Flow Features

Over the wing, the flow separates at the wing leading-edge and subsequently rolls up to form a stable, separation-induced primary vortex. The flow reattaches over the wing induced by leading-edge vortex and the spanwise flow under the primary vortex subsequently separates a second time to form a counter-rotating secondary vortex outboard of the primary one. The simulations results illustrated in Fig. 6a captures also the formation of a tertiary vortex separation with a similar mechanism. In fact, Figure 6a shows an illustration of the vortices plotting the instantaneous Q-criterion iso-surface. The iso-surface is colored by the normalized helicity H_n. The sign of the helicity (positive in blue and negative in red) can be used to separate primary from secondary and tertiary vortices, because it indicates the sense of rotation [14]. The IDDES results in Fig. 6a allow for a qualitative assessment of the resolution of turbulence in the LES areas. Turbulent fluctuations are clearly visible in the vortices and the level of resolution seems to be very high, a large spectrum of turbulent structures appears to be resolved by the grid.

Moreover, at the transonic speed of $Ma = 0.8$ the flow is much more complex compared to subsonic conditions, because the flow above the delta wing reaches supersonic speeds and shock waves appear. Fig. 6b shows two main shocks, a detached shock wave close to the sting tip and a recompression shock wave close to the trailing edge to adjust the pressure level. The interaction between the shock "1" and the leading-edge vortex is highlighted in Fig. 6b because this phenomenon could trigger vortex breakdown already at lower AoA, as discussed by Konrath et al. [4]. It also generates the reduction of velocity and suction over the wing, as it will be confirmed by analysing the mean flow features in Section V.B.

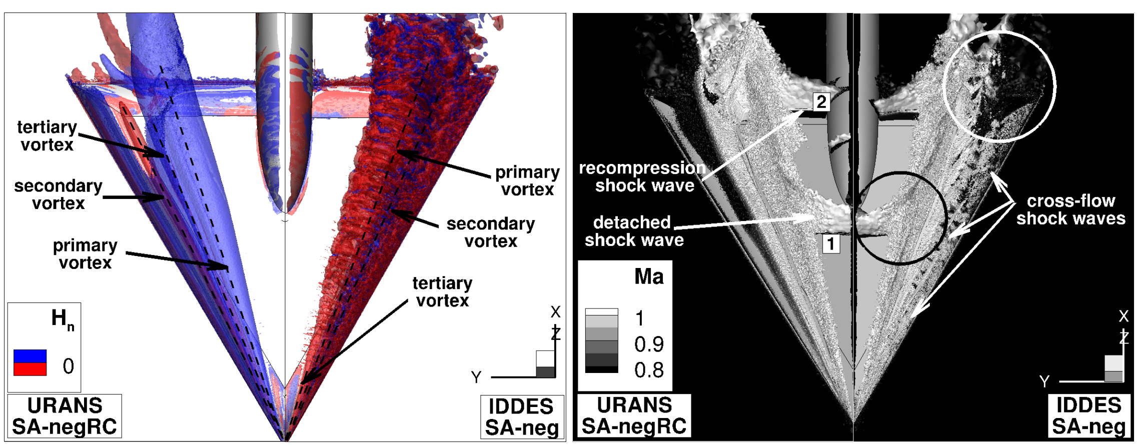

(a) Q-criterion **(b) X-direction density gradient**

Fig. 6 Instantaneous Q-criterion iso-surface with flood contour by normalized helicity H_n and density gradient in x-direction $\nabla\rho_x$ iso-surface with flood contour by Mach number Ma, comparison between URANS and IDDES ($\Delta t = 1e{-6}$) **results for the VFE-2 geometry with** $Ma_\infty = 0.8$, $Re_\infty = 2 \cdot 10^6$, $\alpha = 20.5°$

Fig. 6 shows also that the IDDES approach captures the shear layer emanating from the leading-edge and chaotically transported downstream over the wing close to the trailing edge (highlighted in Fig. 6b). The separated shear layer seams to be not rolling up to form a leading edge vortex over the wing any more, but is transported downstream without inducing additional velocities on the wing surface. This phenomenon abruptly changes the aerodynamic coefficients due to the drop in suction footprint behind the separation, and it could explain the different prediction of the lift coefficient illustrated in Fig. 4.

The direct effect of the vortices is an additional suction footprint over the wing and, consequently, an additional lift which eventually results in a non-linear dependence of the lift force on the angle of attack. The understanding and prediction of the vortex and shock waves, generation and evolution, are of essential importance. The interaction phenomenon between vortex core and shock waves that is crucial for the understanding of the flow physics at transonic conditions needs in particular to be assessed in detail.

B. Mean Flow Features

Fig. 7 shows the mean surface coefficient of pressure on the wing. The suction footprint on the wing surface is mainly caused by the high tangential velocity around the inner vortex core.

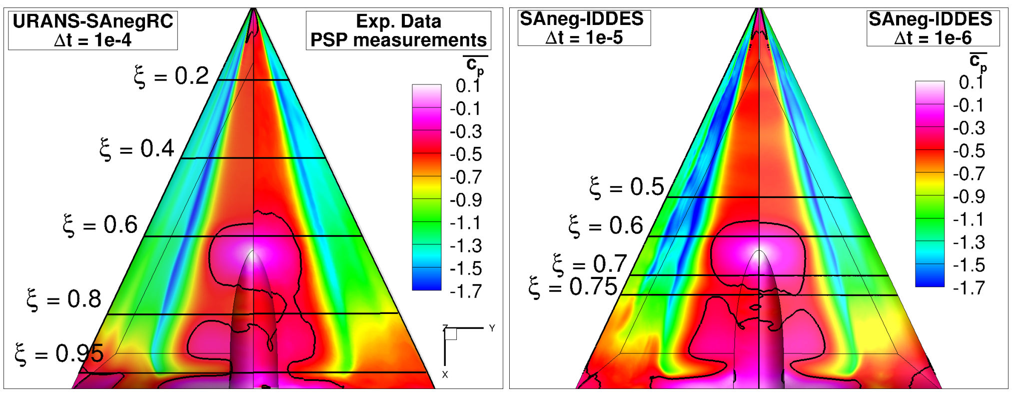

(a) URANS and Experimental Data **(b) IDDES with Δt = 1e−5 s and Δt = 1e−6 s**

Fig. 7 Mean surface coefficient of pressure $\overline{c_p}$, comparison between experimental data, URANS and IDDES results. The black contour lines indicate the sonic pressure coefficient $\overline{c_p^*} = -0.43$.

The investigation of the supersonic area over the wing and, consequently, the presence of the shock waves can be continued taking a look at Fig. 7, in which the sonic pressure coefficient $\overline{c_p^*} = -0.43$ is indicated with the black contour lines. Three main considerations can be done. First of all, the IDDES approach replicates the experimental results best in terms of predicted sonic area over the wing with respect to the experimental data. Secondly, Fig. 7 shows that in front of the secondary vortex a cross-flow shock wave is probably located because the outboard directed flow underneath the primary vortex close to the surface is supersonic. And then the contour lines of the sonic pressure coefficient in the center of the delta wing gives indication of a shock wave in front of the sting fairing, i.e. about $\xi = 0.55$, and a second one closer to the trailing edge downstream of $\xi = 0.8$, not shown in Fig. 6b. Fig. 8 shows the mean surface coefficient of pressure $\overline{c_p}$ distribution at symmetry plane $\eta = 0$, in order to quantify the intensity of the aforementioned shock waves taking a look of the pressure behaviour. Although the simulation results predict an higher pressure peak close to the wing apex ($\xi = 0$) and to the sting tip ($\xi \approx 0.62$), the pressure trend and the position of the shock waves are well captured by the numerical data. The presence of the well-predicted shock wave in front of the sting gives reason to presume the possible occurrence of a vortex breakdown, which may the result from his interaction with the primary vortex.

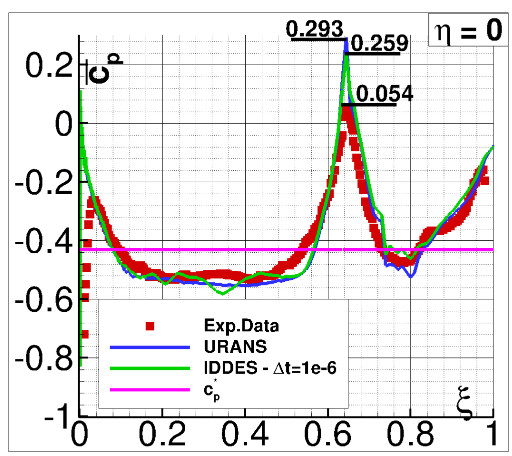

Fig. 8 Mean surface coefficient of pressure $\overline{c_p}$ distribution at symmetry plane $\eta = 0$

In order to analyze this presumption and the prediction of the $\overline{c_p}$ in detail, several slice planes have been extracted, as indicated in Fig. 7a. The $\overline{c_p}$ distribution along the spanwise direction at chordwise positions $x/L = 0.2,\ 0.4,\ 0.6,\ 0.8,\ 0.95$ is plotted in Fig. 9, by doing a comparison between all the available data, experimental and simulation results (URANS, IDDES with Δt = 1e−5 s and Δt = 1e−6 s using the 30M reference mesh and IDDES with Δt = 2e−6 s using the 24M mesh). The comparison is presented in order to prove that the best results are achieved with the IDDES with Δt = 1e−6 s using the 30M reference mesh. In this way, the sensitivity of the results to the temporal and spatial (grid-)resolution is illustrated and discussed.

First of all, the $\overline{c_p}$ distribution confirms that no relevant differences are present between the IDDES results achieved with the 30M and the 24M mesh, as it could have been expected from Fig. 4. For this reason, the IDDES results with the 30M mesh are taken as reference and the uncertainties due to the mesh resolution with respect to IDDES results could be considered significantly reduced.

Fig. 9 in general shows a great agreement between IDDES results (Δt = 1e−6) and experimental data and, in particular, a great prediction of the suction footprint over the wing caused by the presence of the vortices. Hybrid RANS/LES considerably improves the numerical results, although the experimental result are not well reproduced in the front part of the wing. The reasons behind these discrepancies will be explained in Section V.D, where the grey-area issue is addressed.

The secondary and tertiary vortices are graphically visualized due to the smoother peaks of the surface c_p for $\eta \approx 0.7$ and 0.85 at chordwise station $\xi = 0.2$. The tertiary vortex then correctly disappears in the IDDES results with Δt = 1e−6 at chordwise station $x/L = 0.4$ by matching perfectly the experimental data, while it is still wrongly present in the URANS results.

As already said, the best results are achieved with the time step equal to Δt = 1e−6 s by keeping the convective CFL lower than unity, as it has been illustrated in Fig. 5. However, it is very interesting to note that increasing the time step size does not considerably affect the surface $\overline{c_p}$ over the wing caused by the primary vortex prediction. On the other hand, the time step Δt = 1e−5 generates a wrong prediction of the secondary and the tertiary vortex due to large unsteady fluctuations of these phenomena.

As it can be seen in Fig. 9 at chordwise $\xi = 0.95$ (close to the trailing edge), the IDDES approach captures the shear layer emanating from the leading-edge and chaotically transported downstream over the wing not rolling up any more to form a stable leading-edge vortex over the wing. This phenomenon has been highlighted in Fig. 6b as well. The suction footprint behind the transported shear layer leading-edge separation abruptly drops because the vortex loses kinetic energy. The primary vortex is no longer fed by the generated turbulence, the coherent vortex condition is not sustainable and it tends to break down.

The experimental data [4] indicate the presence of the vortex breakdown in the rear part of the wing. The breakdown onset position is predicted slightly too far downstream on the wing by the IDDES results. There could be different reasons behind the discrepancies between the measured and the simulated vortex breakdown‘s strength or intensity. Two possible options could be the shock-vortex interaction and the grey-area issue. After having validated the simulation results with the experimental data, the vortex pattern and the aforementioned phenomena will be analysed in the following work by investigating the IDDES results with Δt = 1e−6.

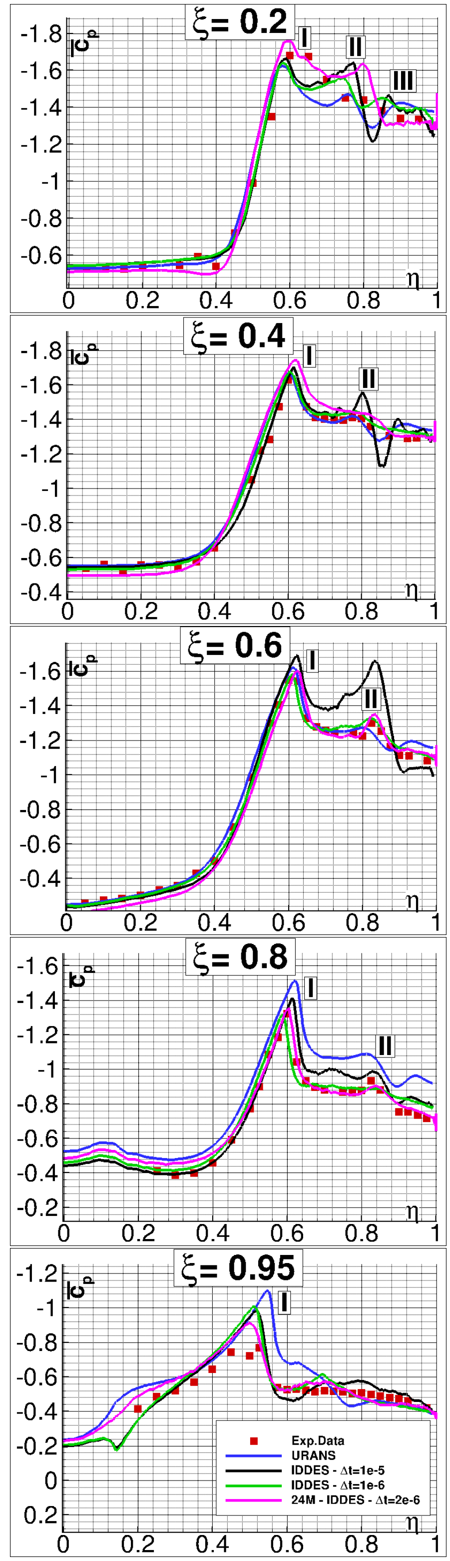

Fig. 9 Mean surface $\overline{c_p}$ distribution at chordwise locations x/L = 0.2, 0.4, 0.6, 0.8, 0.95 comparison between experimental data, URANS and IDDES results

C. Vortex Pattern and Vortex-Shock Interaction

First of all, the vortex pattern itself and how it is modified taking the shock-vortex interaction into account need to be understood in detail. Because of this purpose, several additional plots are provided. Fig. 10 shows the mean x-direction vorticity $\overline{\omega_x}$ distribution at chordwise locations $\xi = 0.5,\ 0.6,\ 0.7,\ 0.75$ by doing a comparison between experimental data and IDDES results. Moreover, Fig. 11 shows the mean density gradient magnitude $||\overline{\nabla \rho}||$, the normalized mean x-direction velocity $\overline{u}/U_\infty$ and the normalized mean in-plane tangential velocity $\overline{u_\theta}/U_\infty$ distribution by taking IDDES results at chordwise locations $\xi = 0.5,\ 0.6,\ 0.7,\ 0.75$, close to the first shock wave location, into account.

The detached shock, also called a bow shock, caused by the sting tip and illustrated in Fig. 6 interacts with the leading-edge vortex core and generates a decrease in the x-velocity within the vortex core (see Fig. 11 at chordwise $\xi = 0.7$) with a subsequently suction footprint reduction observable in Fig. 9 at chordwise station $\xi = 0.8$. The vortex core loses velocity and kinetic energy across the shock wave. This phenomenon is not well captured by the URANS results that show a larger deviation with the experimental data in the rear part of the wing with respect to the IDDES ones.

The unburst vortex is characterized in general by a coherent structure with high values of axial and rotational velocity in which the vorticity increases along the axial direction. However, as it can be seen in Fig. 10 by comparing in particular the results at chordwise station $\xi = 0.6$ and $\xi = 0.7$, the x-direction vorticity tends to dissipate and, consequently the vortex tends to break down, after the discussed interaction with the shock wave in front of the sting fairing ($\xi = 0.62$).

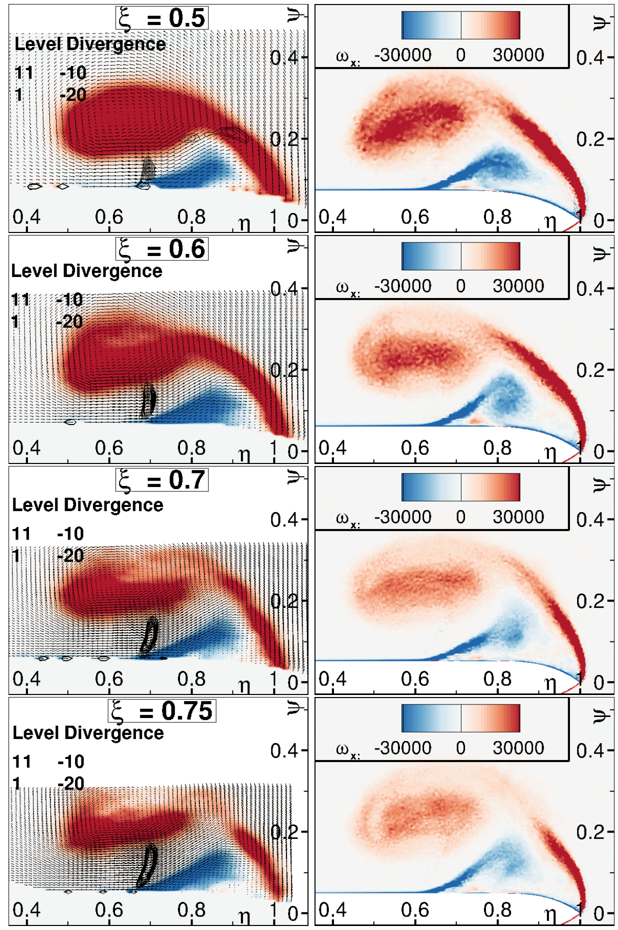

Fig. 10 Mean x-direction vorticity $\overline{\omega_x}[1/s^2]$ distribution at chordwise locations $\xi = 0.5,\ 0.6,\ 0.7,\ 0.75$ comparison between experimental data (left) and IDDES results (right). The block contour lines in the experimental data are related to the divergence of the in-plane velocity vectors, $\nabla \cdot \vec{u}[1/s^2]$.

Since a vortical structure comes from the concentration of the low energy parts of the flow, initially contained in the boundary layer, the vortex can also be seen as a region of rotational flow whose stagnation conditions, especially the pressure, are inferior to those of the outer field. Thus the vortex is like an energy 'hole' or entropy 'hill' which will be more sensible to disturbing entities, the situation being similar to that of a boundary layer [15].

One of the parameters of the vortex breakdown's formation is the influence of tangential speed and axial velocity along the core of the vortex. In intense vortices forming over a delta wing at high incidence, the value of the velocity axial component u_{axial} is greater than the outer value u_{ext}. At these flow conditions the u_{axial} exceeds u_{ext} by a factor of 2, as it is shown by the $\overline{u}$ in Fig. 11. Moreover, the $\overline{u_\theta}$ in Fig. 11 shows that, in the outer part of the vortex structure, the flow tends towards irrotational behaviour for which $u_\theta \sim 1/r$. On the other hand, near the vortex centre-line, in the vortex core, where the viscosity plays a major role, the tangential velocity distribution has a solid body rotation shape for which $u_\theta \sim r$. Between the two regions exists a transition zone ensuring a continuous evolution of the velocity profile. This is exactly what induces a static pressure dip in the centre of the vortical structure whose depth depends on the magnitude of the tangential velocity u_θ [15].

The strength of the vortex can be characterized by the swirl ratio or Rossby number, formulated in Eq. 3. It likens the respective amplitudes of the swirling and axial motions, by comparing the axial velocity (u_{axial}) in the vortex core with the maximum swirl velocity ($\max(u_\theta)$). Since the breakdown mechanism involves the local properties of the velocity distributions, the Rossby number can be used to analyze the occurrence of vortex breakdown.

$$Ro = \frac{u_{axial}}{max(u_\theta)} \tag{3}$$

The decline in the value of Rossby number has the meaning of increased vortex intensity and it further affects the vortex vulnerability. By making an oversimplification of the reality, the criterion of Rossby number applies to most cases of a vortex in the delta wing with values between 0.9 and 1.4. The value higher than 1.4 indicates the level of stability of the vortex and the value below 0.9 indicates the occurrence of a vortex breakdown [15].

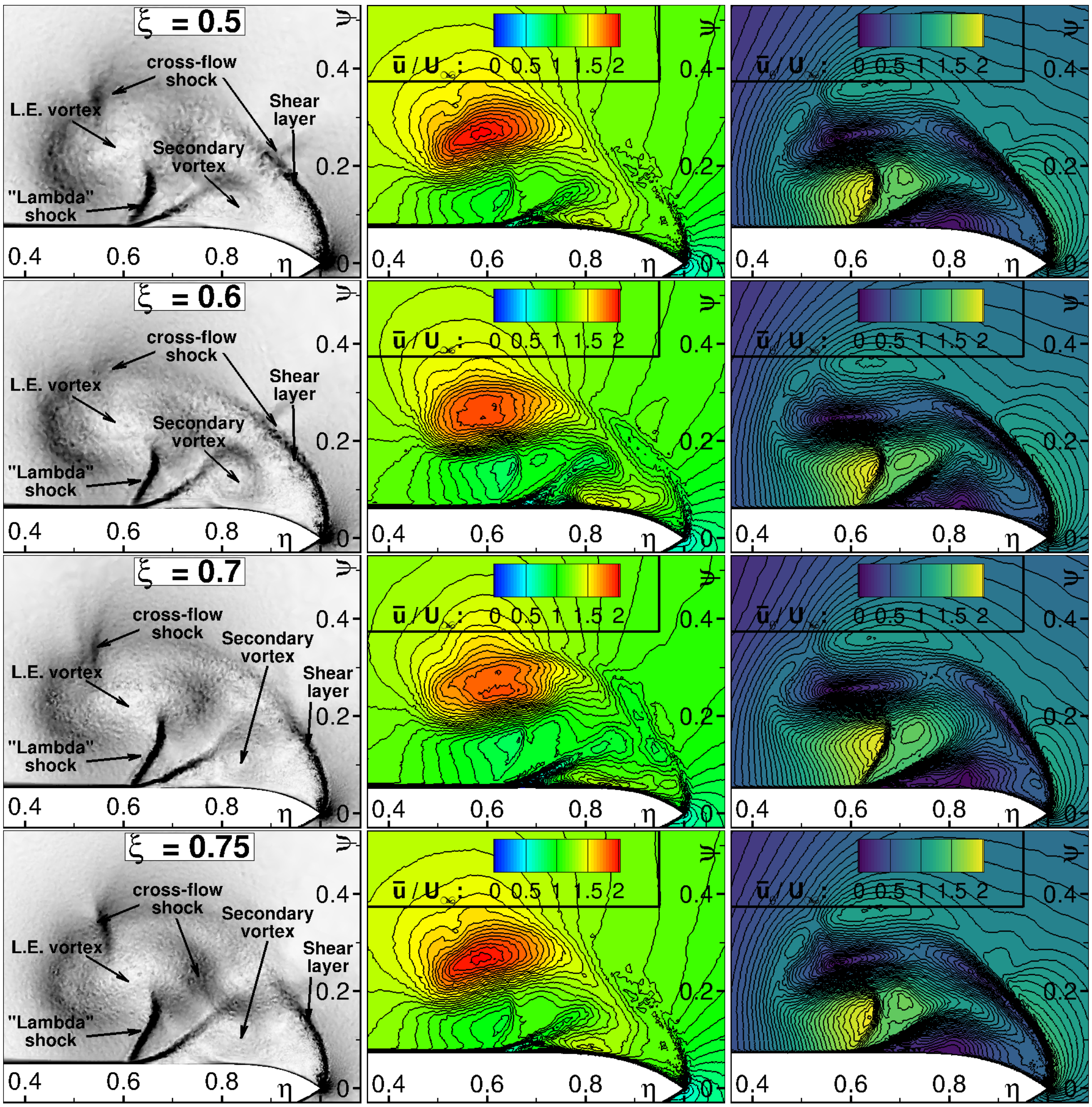

Fig. 11 Mean density gradient magnitude $||\nabla\rho||$, mean normalized x-direction velocity $\overline{u}/U_\infty$ and mean normalized in-plane tangential velocity $\overline{u_\theta}/U_\infty$ distribution, IDDES results at chordwise locations $\xi = 0.5,\ 0.6,\ 0.7,\ 0.75$

It is worthy to consider that the width of the shock wave is of the same order of the magnitude as the local mean free path of fluid particles. The shock wave can be regarded as a sharp discontinuity in common aerodynamic flow and, across the shock, the Mach number, the normal velocity and, subsequently, the Rossby number, suddenly drop. For this reason, it can be affirmed that, at these flow conditions and at this location, the shock wave is not strong enough to abruptly trigger the vortex breakdown. In fact, the shock wave intensity increases on the wing close to the sting tip as the angle of attack rises, since it is directly proportional to the incoming Mach number (and velocity). For this reason, in particular at transonic conditions, the increase of the angle of attack may thus induce the vortex breakdown in correspondence of the area where the interaction between the vortex core and the shock wave is located. If, like in this case, the shock wave is not strong enough to induce a vortex breakdown, after the interaction with the aforementioned shock, the leading-edge vortex tends to recover its stability by overcoming the perturbation. The x-velocity of the vortex starts consequently to increase again in the vortex core, as it is shown in Fig. 11 by doing the comparison between the results at chordwise stations $\xi = 0.7$ and $\xi = 0.75$.

In Fig. 10 are also plotted the negative values of the divergence of the in-plane velocity vectors ($\nabla \cdot \vec{u}$) which gives an indication of the location and shape of a cross-flow shock wave in the experimental results. The distribution of $\overline{u_\theta}$ is altered by the presence of these shocks, as it can be seen from the iso-contour lines of $\overline{u_\theta}$ in Fig. 11. The mean density gradient magnitude $||\nabla\rho||$ plot in Fig. 11 shows that the leading-edge vortex presents a "kidney-shape" for $Ma = 0.8$ and confirms that some cross-flow shock waves appear, since several regions of high values of $||\overline{\nabla\rho}||$ are identified. These shock waves are present around the leading-edge vortex and on the top of the shear layer and they are likely to be caused by the curvature of the trajectory of the flow causing the flow to accelerate up to thermophysical conditions which cannot be sustained [16]. Moreover, a complex shock-waves system is located beneath the leading-edge vortex. The "lambda" shock located beneath the leading-edge vortex is caused by the acceleration of the cross-flow in this region and its presence deeply alters the local flow topology. Owing to the interaction of this shock with the boundary layer developing on the upper side of the wing, the flow detaches and feeds the secondary vortex [16].

D. Turbulence-related Variables

Fig. 12 shows the contours of $R_t = \mu_t/\mu$ are plotted, where μ is the molecular dynamic viscosity. The modeled turbulent eddy viscosity, μ_t, is compared at chordwise locations $\xi = 0.2,\ 0.6,\ 0.95$ between URANS and IDDES. The URANS approach has produced overall higher levels of turbulent eddy viscosity in the vortex core. In general, the region with large μ_t values in RANS computations corresponds to vortex motions with relatively high turbulence energy generation in relation to strong flow rotation and deformation [2]. As it can be seen in Fig. 12, the RC-correction avoids the excessive eddy viscosity production in the front part of the wing. Unfortunately, it is not sufficient in the rear part and in the vortex region, where the turbulent viscosity production is incredibly large.

Regarding the hybrid RANS-LES run, it is worthy to recall Fig. 3 that shows the instantaneous hybrid length scale over RANS length scale ($\tilde{d}/d$). The IDDES approach employs the SGS eddy viscosity in the off-wall region and the IDDES R_t-contours show that the SGS eddy viscosity is much smaller than its RANS counterpart. The relatively low level of modelled μ_t in LES is associated with the local fine grid resolution required for LES. On the other hand, the region with large μ_t in LES mode indicate strong local flow rotation/deformation and/or coarse grid resolution, inducing usually intensive energy dissipation of resolved large-scale turbulence [2]. For this reason, a slight grid refinement could be performed in the rear part of the wing close to the leading edge where the shear layer separates and rolls up.

Besides, since the modelled μ_t level is related to the modelled or resolved turbulent generation/dissipation and diffusion, it is reflected in the resolved turbulent kinetic energy, K. As shown in Fig. 12 at $\xi = 0.2$, the resolved turbulent kinetic energy, K, is significantly under-predicted in the initial development of the vortical flow. The initial development of resolved turbulence is somewhat delayed because the LES-resolved turbulence is insufficient in the initial stage of the vortical flow. This phenomenon is the so-called grey-area problem rooted in the IDDES modeling and it affects the downstream development of the turbulent process, including vortex breakdown onset position. The "grey-area" problem, for which the resolved turbulence in the shear layer by the LES mode is much less saturated, happens due to the fact that the formation of the vortex is supported by a process of "rolling-up" and "wrapping" of near-wall layers that are modeled by the RANS mode. In other words, the transition of the shear layer between the RANS and the LES mode should be the main reason for some discrepancies highlighted in the $\overline{c_p}$ results in the front part of the wing and it generates a rather "stiff" resolved vortex motion leading to a delayed vortex burst and breakdown.

Moroever, the resolved turbulent kinetic energy, K, at $\xi = 0.95$ shows the separated shear layer and chaotically transported downstream close to the leading edge, whereas a cross-flow shock alters the K distribution below the primary vortex.

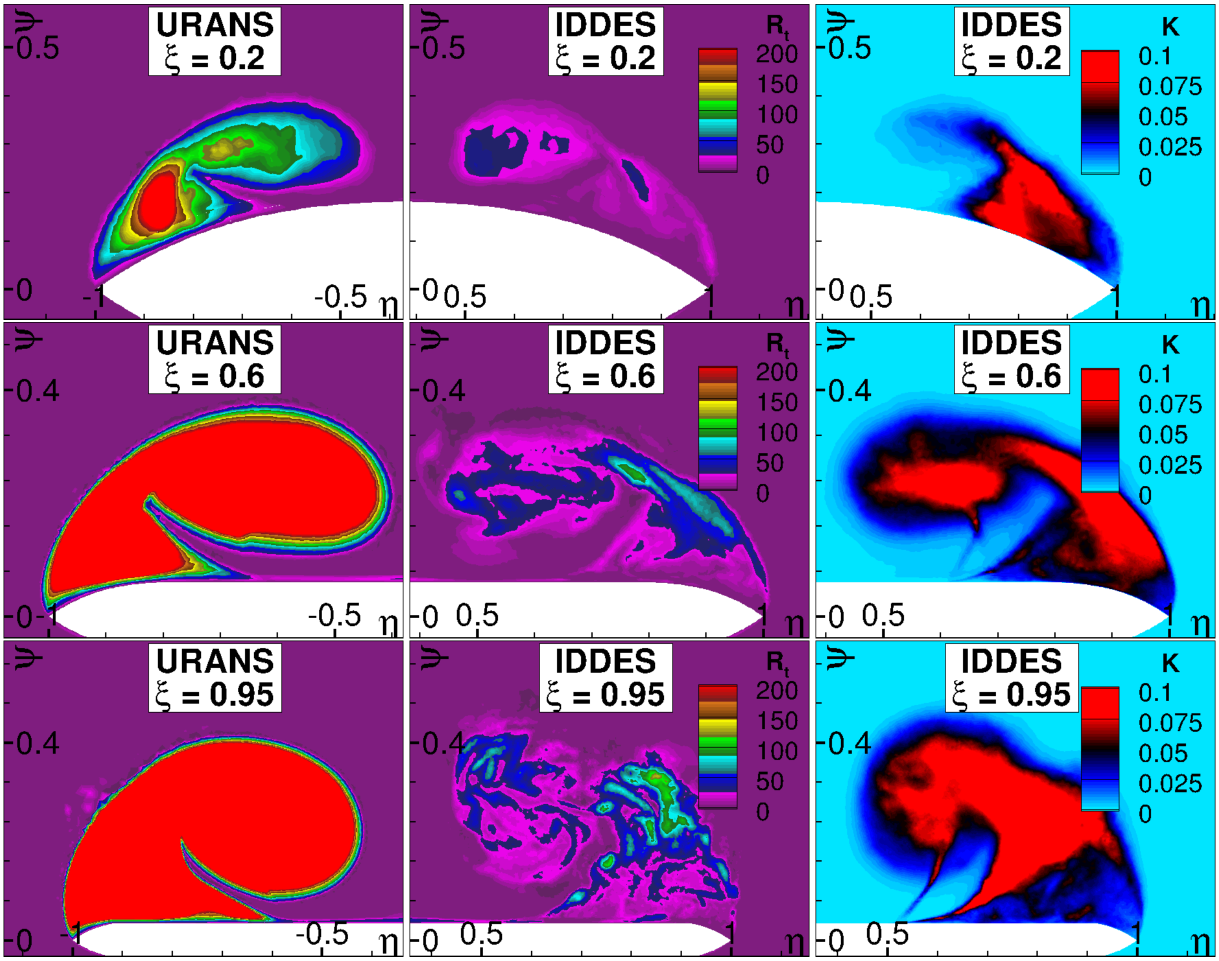

Fig. 12 Instantaneous turbulent eddy viscosity, represented by R_t, and resolved turbulent kinetic energy K, normalized by U_∞, at chordwise locations $\xi = 0.2,\ 0.6,\ 0.95$, comparison between URANS and DDES results

VI. Conclusions

The qualitatively and quantitatively illustrated results show that all the computational time spent on IDDES has been worth the effort also in order to provide a contribution in the progress of the hybrid method. The IDDES with an adequate cell and time step size shows most of the important flow features and represents a valid method in order to improve the physics understanding within this research field. The sensitivity of the results to temporal and spatial resolution has been addressed and commented upon in Section V.B leading to important considerations, that have never been demonstrated with the presented accuracy.

The demonstration and the understanding of the multiple flow physics phenomena that occur over the wing at transonic speed condition were the purpose of the present work. The pressure trend and the position of the shock waves are well captured by the numerical data. The hybrid method is able to capture the interaction between the leading-edge vortex and the shock waves generated by the transonic free stream flow conditions, as it has been discussed in Section V.C. It as been shown and explained in detail as this phenomenon could trigger the vortex breakdown and what happens over the wing (in particular within the vortex core) with a promising accuracy. However, it has been proved in Section V.D that the initial development of resolved turbulence is somewhat delayed because of the LES-resolved turbulence. K is insufficient in the initial stage of the vortical flow and affects the downstream development of the turbulent process, including vortex breakdown onset position, which has been predicted slightly too far downstream on the wing by the IDDES results.

Since IDDES appears to be a promising tool to simulate the flow physics around a delta wing at transonic conditions, even at more challenging conditions and configurations. In order to continue this analysis, further steps will focus on the unsteady behaviour of the hybrid results by investigating the Reynolds stress. The spectral-temporal analysis is surely helpful to investigate the unsteadiness as well.

Moreover, the conducted study on the CFL condition suggests that an "adaptive" and local time scale method could also be used to speed-up the simulation and save computational resources.

Finally, other potential hybrid modelling approaches (alternative to the IDDES model) could be taken for further studies into account. Further improvements of the hybrid RANS/LES methods could lead for example to creation of a high-fidelity database in order to conduct aircraft design and to improve cheaper RANS based models with the help of machine learning tools.

Acknowledgments

The funding of this investigation by Airbus Defence and Space within the project "Efficient Turbulence Modelling for Vortical Flows from Swept leading-edges" is gratefully acknowledged.

The authors gratefully acknowledge the German Aerospace Center (DLR) for providing the DLR TAU-Code used for the numerical investigation of the present research.

Furthermore, providing the meshing software by Ennova Technologies Inc. is sincerely appreciated.

The authors thank to the Gauss Centre for Supercomputing for funding this project by providing computing time on the GCS Supercomputer SuperMUC at Leibniz Supercomputing Center (account number pn29xa).

References

[1] Moioli, M., Breitsamter, C., and Sørensen, K., "Turbulence Modeling for Leading-Edge Vortices: an Enhancement based on Experimental Data," AIAA SciTech Forum, Orlando, FL, 2020. https://doi.org/10.2514/6.2020-1032.

[2] Peng, S.-H., "Verification of RANS and Hybrid RANS-LES Modelling in Computations of a Delta-Wing Flow," 46th AIAA Fluid Dynamics Conference, Washington, D.C.", 2016. https://doi.org/10.2514/6.2016-3480.

[3] Cummings, R. M., and Schütte, A., "Detached-Eddy Simulation of the vortical flow field about the VFE-2 delta wing," *Aerospace Science and Technology*, Vol. 24, No. 1, 2013, p. 66–76. https://doi.org/10.1016/j.ast.2012.02.007.

[4] Konrath, R., Klein, C., and Schröder, A., "PSP and PIV Investigations on the VFE-2 Configuration in Sub- and Transonic Flow," 46th AIAA Aerospace Sciences Meeting and Exhibit, Reno, Nevada, 2008. https://doi.org/10.2514/6.2008-379.

[5] Sagaut, P., Deck, S., and Terracol, M., *MULTISCALE AND MULTIRESOLUTION APPROACHES IN TURBULENCE. LES, DES and Hybrid RANS/LES Methods: Applications and Guidelines*, 2nd ed., Imperial Collegre Press, 2013, Chap. 7, pp. 286–292. https://doi.org/10.1142/p878.

[6] Langer, S., Schwöppe, A., and Kroll, N., "The DLR Flow Solver TAU - Status and Recent Algorithmic Developments," 52nd Aerospace Sciences Meeting, National Harbor, Maryland, USA, 2014. https://doi.org/10.2514/6.2014-0080.

[7] Kölzsch, A., "Active Flow Control of Delta Wing Leading-Edge Vortices," PhD dissertation, TUM, Chair of Aerodynamics and Flow Mechanics, 2017.

[8] Landa, T., Klug, L., Radespiel, R., Probst, S., and Knopp, T., "Experimental Analysis of the Interaction between Streamwise Vortices and a High-Lift Airfoil," 2019. https://doi.org/10.2514/6.2019-0576.

[9] Spalart, P. R., and Allmaras, S. R., "A One-Equation Turbulence Model for Aerodynamic Flows," AIAA, 30th Aerospace Sciences Meeting and Exhibit, Reno, NV, 1992. https://doi.org/10.2514/6.1992-439.

[10] Rumsey, C., *The Spalart-Allmaras Turbulence Model, Turbulence Modeling Resource*, NASA Langley Research Center, 2021.

[11] Shur, M. L., and al., "Turbulence Modeling in Rotating and Curved Channels:Assessing the Spalart-Shur Correction," *AIAA Journal*, Vol. 38, No. 5, 2000. https://doi.org/10.2514/2.1058.

[12] Probst, A., and Reuß, S., "PROGRESS IN SCALE-RESOLVING SIMULATIONS WITH THE DLR-TAU CODE," Deutscher Luft- und Raumfahrtkongress, Braunschweig, Deutschland, 2016.

[13] Spalart, P. R., *Young-Person"s Guide to Detached-Eddy Simulation Grids*, NASA Langley Technical Report Server, 2001.

[14] Levy, Y., Degani, D., and Seginer, A., "Graphical visualization of vortical flows by means of helicity," *AIAAJ*, Vol. 28, No. 8, 1990. https://doi.org/10.2514/3.25224.

[15] Delery, J. M., "Aspects of vortex breakdown," *Progress in Aerospace Sciences*, Vol. 30, No. 1, 1994, p. 1–59. https://doi.org/10.1016/0376-0421(94)90002-7.

[16] Riou, J., Garnier, E., and Basdevant, C., "Compressibility effects on the vortical flow over a 65° sweep delta wing," *Physics of Fluids*, , No. 3, 2010, pp. 35–102. https://doi.org/10.1063/1.3327286.